Bifunctional Zinc-Molybdate or Zinc molybdenum Oxide/Metal-Nitrogen-Carbon catalytic layers with improved four-electron selectivity for oxygen reduction in acidic medium

Aaron Roy, Leonardo Girardi, Dario Mosconi, Moulay Tahar Sougrati, Deborah Jones, Stefano Agnoli, Frédéric Jaouen

Bifunctional Zinc-Molybdate or Zinc Molybdenum Oxide/Metal-Nitrogen-Carbon Catalytic Layers with Improved Four-Electron Selectivity for Oxygen Reduction in Acidic Medium

Aaron Roy[1], Leonardo Girardi,[2] Dario Mosconi[2], Moulay Tahar Sougrati[2], Deborah Jones[1], Stefano Agnoli[2 (*)], Frédéric Jaouen[1 (*)]

[1] ICGM, Univ. Montpellier, CNRS, ENSCM, Montpellier, France

[2] Dipartimento di Scienze Chimiche and INSTM Research Unit, Università degli Studi di Padova, Padova, Italy

(*) Corresponding authors.

Stefano Agnoli, stefano.agnoli@unipd.it

Frédéric Jaouen, frederic.jaouen@umontpellier.fr

Abstract

Platinum-group-metal-free metal-nitrogen-carbon catalysts for the oxygen reduction reaction have demonstrated high initial activity and power performance in proton exchange membrane fuel cells. The main challenge facing this class of catalysts is their poor durability in operating acidic fuel cells. Their key *operando* degradation mechanisms involve oxidative attacks triggered by the catalysis of the oxygen reduction on atomically-dispersed 3d transition metals. Reactive oxygen species such as H_2O_2 or radical species are particularly aggressive to the carbon matrix. Minimizing H_2O_2 by-product formation during oxygen reduction or actively scavenging any formed H_2O_2 are therefore promising routes to improve their durability.

Here, we report that Zn-molybdate and Zn molybdenum oxide have low activity towards H_2O_2 decomposition and electro-reduction in acid, but result in a strong synergistic effect with various M-N-C catalysts. The addition of α-$ZnMoO_4$ or $Zn_3(OH)_2(MoO_4)_2$ in cathode layers resulted in improved four-electron ORR selectivity of M-N-C catalysts (M = Fe, Co, Cr) as well as moderately improved durability in accelerated stress tests in O_2-saturated pH 1 electrolyte. The improvement in selectivity could be rationalized by hydrogen peroxide electro-reduction measurements and catalase enzyme-like activity tests. Both types of measurements revealed higher reactivity towards H_2O_2 scavenging when Metal-N-C catalysts are physically mixed (in a catalytic layer) or together in a suspension in solution with Zn-molybdate or Zn molybdenum oxide, revealing a synergy effect. Control experiments with $ZnCl_2$ and Na_2MoO_4 salts however suggest that leached ions from $ZnMoO_4$ in acidic solution are likely at the root of the synergy effect.

1. Introduction

Platinum-group-metal (PGM)-free catalysts for the oxygen reduction reaction (ORR) have been intensively developed in the last decade, resulting in significant advances in their initial activity and power performance in proton exchange membrane fuel cells (PEMFC). [1-4] However, while some Fe-N-C catalysts with atomically-dispersed FeN_x sites have met intermediate targets defined by the United States Department of Energy (< 40% decrease in ORR activity after 10,000 load cycles), [5] this high stability in acidic conditions was achieved in O_2-free environments. Comparative studies with and without O_2 in the cathode environment showed that the introduction of O_2 during load-cycling (therefore triggering the ORR) resulted in dramatically enhanced ORR activity loss. [6,7] This was observed in both a rotating disk electrode (RDE) setup and in PEMFC, and implies that the stability of Fe-N-C in acidic medium is a necessary, but insufficient condition for their successful practical implementation. This recent conclusion highlights the difference between PGM-based catalysts, for which the key *operando* degradation mechanisms do not involve O_2 nor the ORR (platinum dissolution, particle growth via Ostwald ripening), and PGM-free acid-stable catalysts for which the key *operando* degradation mechanisms are directly or indirectly related to the presence of O_2 or the occurrence of the ORR. Examples for indirect relations with O_2 or ORR are the attack by H_2O_2 or other more reactive oxygen species (ROS) [8] and ROS-induced carbon corrosion. [6] The demetallation of Fe from FeN_x sites in acidic medium was shown to be triggered or strongly accelerated when Fe-N-C materials catalyze the ORR. This has been shown both with model FeN_4 sites such as Fe-phthalocyanines and with pyrolyzed Fe-N-C catalysts comprising Fe mainly as FeN_x sites formed during pyrolysis. [5, 9] The long-recognized, but not well-understood drawback of Fenton reactions in acidic medium between PGM-free catalysts comprising a 3d transition metal and H_2O_2 is a fundamental issue for durable PGM-free cathodes in PEMFC. Hitherto, this challenge has been faced by i) developing M-N-C catalysts with high selectivity for four-electron ORR, ii) replacing Fe with another metal such as Co, Mn or Sn, [10-12] or iii) adding radical scavengers onto the M-N-C catalyst or in the cathode active layer. [13] However,

these approaches have hitherto not led to satisfactory durability in operating PEMFC. While some M-N-C catalysts have shown high initial selectivity in rotating ring disk electrode (RRDE) setup, a study showed that exposing such catalysts to a small amount of H_2O_2 progressively decreases their selectivity during ORR, thereby defining an evil circle of deactivation. [8] Concerning the nature of the transition metal in M-N-C, while Fe cations are commonly regarded as the most active for Fenton reactions, other 3d transition metals (either as MN_x sites or as metal species resulting from MN_x degradation) can also be active. For example, a study on 3d metal cations performed in neutral pH showed that Cu(II), Cr(III) and Co(II) can produce more ROS than Fe(III). [14] In addition, Co-N-C catalysts have generally lower four-electron ORR selectivity than Fe-N-C, [15] which would partially offset the expected benefit of the alleged lower Fenton reactivity of Co-N-C vs. Fe-N-C, due the higher production rate of H_2O_2 for a fixed current density of the PEMFC. Last, radical scavengers such as CeO_2 can decrease the concentration of ROS, but do not scavenge H_2O_2, which is the source of ROS for M-N-C systems.

Functionalizing M-N-C catalysts or M-N-C catalytic layers with active sites that can electrochemically reduce H_2O_2 to water or chemically decompose it into O_2 and water is therefore a promising strategy for improved durability. This bifunctionality concept was investigated for example by Mechler *et al.* by adding a small amount of platinum nanoparticles (1-2 wt%) onto Fe-N-C catalysts. [16] While this resulted in dramatically improved durability in PEMFC while keeping the same apparent activity for Fe-N-C and Pt/Fe-N-C (suggesting Pt did not contribute to the initial activity, but only impacted the durability of FeN_x sites), a subsequent study showed that the annealing step applied for reducing the Pt salt to Pt NPs resulted in core-shell particles comprising a Pt core and a Fe_2O_3 shell. [17] While such core-shell particles have lower ORR specific activity than exposed Pt NPs, their ORR specific activity is significant when the Fe_2O_3 shell is thinner than 1 nm. In addition, the Fe_2O_3 shell on top of Pt resulted in the deactivation of Pt for the electroreduction of H_2O_2. As a consequence, the concept of improved durability of FeN_x sites by the addition of a H_2O_2 decomposing catalyst could not be unambiguously demonstrated in that work. Moreover, a content of 1-2 wt % Pt onto Fe-N-C combined with loadings

of 4 mg $_{Fe\text{-}N\text{-}C}$ ·cm^{-2} leads to cathode loadings of 40-80 μg_{Pt}·cm^{-2}. Similar or even higher PEMFC performance can be obtained with Pt catalysts at such low Pt loading, without resorting to Fe-N-C. [18]

Thus, while the concept of adding a PGM-free catalyst to M-N-C for the active removal of *operando* formed H_2O_2 is conceptually attractive, there are no known PGM-free catalysts with significant activity toward H_2O_2 electroreduction or decomposition in acidic medium. Metal-carbides and metal-oxides based on W, Mo, Ti and Sn are stable in the acidic conditions of PEMFC within the typical cathode potential range, but have no or little reactivity toward H_2O_2. Metal-molybdates comprising a divalent metal cation (general formula $MMoO_4$, or $M_xM'_{1-x}MoO_4$ for trimetallic systems, in which M and M' can be a 3d transition metal or an alkaline earth metal of group 2A) are an interesting class of materials with specific properties provided by M (M') for optical, [19,20] catalytic, [21-25] and electrochemical energy storage applications. [26,27] In particular, $ZnMoO_4$ has photocatalytic, [28] optical and antibacterial properties, [29-31], and has been investigated also as an anode material for rechargeable lithium-ion battery. [32,33]

Here, we report that α-$ZnMoO_4$, and $Zn_3(OH)_2(MoO_4)_2$ derived from α-$ZnMoO_4$ by peroxide treatment, supported on carbon or nitrogen-doped carbon have *per se* low activity towards H_2O_2 decomposition and H_2O_2 electro-reduction in acid, but a strong synergistic effect is observed when they are combined with M-N-C catalysts comprising single-metal-atom sites. The addition of α-$ZnMoO_4$ or $Zn_3(OH)_2(MoO_4)_2$ in cathode layers resulted in improved four-electron ORR selectivity of various M-N-C catalysts (M = Fe, Co, Cr) in RRDE setup, as well as moderately improved durability in accelerated stress tests in O_2-saturated pH 1 electrolyte. The improvement in selectivity could be rationalized by hydrogen peroxide electro-reduction measurements and with catalase enzyme-like activity tests. Both types of measurements revealed higher reactivity towards H_2O_2 scavenging when Metal-N-C catalysts are physically mixed (in a catalytic layer) or added together in a suspension in solution with Zn-molybdate, revealing a synergy effect. Control experiments with $ZnCl_2$ and Na_2MoO_4 salts however suggest that leached ions from $ZnMoO_4$ in acidic solution are likely at the root of the synergy effect

between atomically dispersed Metal-N_x sites and large Zn molybdate or Zn molybdenum oxide particles.

2. Experimental Methods

2.1. Material synthesis

2.1.1. Synthesis of $Zn_3(OH)_2(MoO_4)_2$

The α-$ZnMoO_4$ was purchased from Sigma Aldrich (99.9 %) and was converted to $Zn_3(OH)_2(MoO_4)_2$ as follows. Approximately 4 g of α-$ZnMoO_4$ was dispersed in 10 mL of deionized water and placed in an ultrasonic bath for 5 minutes. 1 mL of 30 % (v/v) H_2O_2 solution (Sigma Aldrich) was then added to the α-$ZnMoO_4$ dispersion and left at room temperature under continuous stirring for 24 h. After 24 h, the dispersion was filtered and rinsed several times with deionized water then dried in air at 80° C overnight.

2.1.2. Synthesis of Fe-N-C, Co-N-C and Cr-N-C

Nitrogen doped carbon was synthesized from zeolitic imidazole framework ZIF-8 (Basolite® Z1200 Sigma Aldrich). First, 1.6 g of ZIF-8 was added to a 45 mL zirconia grinding bowl with 100 zirconia grinding balls with diameter 5 mm. The precursor was then ball milled at a rotation of 400 RPM for 4 cycles each of 30 min. Next, the precursor was inserted in a horizontal quartz reactor pre-heated to 1050 °C and purged in Ar. A flash pyrolysis was performed for 1 hour and the quartz reactor was then quenched to room temperature. The N-doped carbon product is labelled N-C. Metal coordination on N-C was performed by first mixing 0.5 g of N-C with $MeCl_2$ (98% anhydrous Sigma Aldrich) to give a total metal loading on NC of 1.0 wt. %. The N-C-flash and $MeCl_2$ precursor were added to a 45 mL zirconia grinding bowl with hundred 5-mm diameter zirconia grinding balls and then ball milled at a rotation of 500 RPM for 4 cycles each at 30 min. After milling, the catalyst precursor was inserted in a horizontal quartz reactor pre-heated to 800 °C and purged in Ar. A flash pyrolysis was performed in Ar with a dwell time of 1 hour, after which the quartz reactor was quenched to room temperature.

2.1.3. Synthesis of $Fe_{0.5}$

$Fe_{0.5}$ was prepared by mixing zeolitic imidazole framework ZIF-8 (Basolite® Z1200 Sigma Aldrich), 1,10-phenanthroline (Sigma Aldrich), and anhydrous Fe(II) acetate (Sigma Aldrich) with a mass ratio of ZIF-8:1,10-phenanthroline of 4:1. Fe(II) acetate was added to give a total iron content of 0.5 wt. % in the precursor mixture. 1.0 g of the precursor mixture was added to a 45 mL zirconia grinding bowl with 100 5-mm zirconia grinding balls then ball milled at a rotation of 400 RPM for 4 cycles each at 30 minutes. Next, the precursor was inserted in a horizontal quartz reactor pre-heated to 1050 °C and purged in Ar. A flash pyrolysis was performed for 1 hour and the quartz reactor was quenched to room temperature

2.2. Electrochemical measurements in RRDE and RDE setups

2.2.1. ORR activity and peroxide yield measurement in RRDE

Catalyst inks were prepared using an ionomer to carbon mass ratio of 0.5. Nafion 1100 EW perfluorosulfonic acid solution (5 wt. % in aliphatic alcohols containing 15- 20 % H_2O, Sigma Aldrich) was added to a suspension of catalyst (either carbon, N-C or M-N-C or a physical mixture of 90 wt % carbon, N-C or M-N-C with 10 wt% α-$ZnMoO_4$ or $Zn_3(OH)_2(MoO_4)_2$) in 1-propanol with a carbon concentration of 2 wt. %. The inks were sonicated in an ultrasonic bath at 20° C for 1 h prior to being drop-cast on the working electrode, to give a total carbon loading of 800 $\mu g \cdot cm^2$, unless otherwise stated. Electrochemical measurements were performed in a 3-electrode cell using a graphite counter electrode and reversible hydrogen reference electrode. ORR polarization curves were performed using a glassy carbon working electrode with platinum ring held at a constant potential of 1.3 V *vs.* RHE. Polarization curves were measured in O_2 saturated 0.5 M H_2SO_4 (prepared from Merck 98% Merckmillipore) at a scan rate of 2 $mV \cdot s^{-1}$ starting from OCP then scanned from 0 to 1 V *vs*. RHE with a rotation speed of 1600 RPM. Prior to ORR measurements a catalyst break-in procedure was performed where the working electrode was cycled at 20 $mV \cdot s^{-1}$ in N_2 saturated electrolyte until negligible change in capacitance was observed. We always report the current density, i.e. the current divided by the geometric area of the working electrode.

2.2.2. PRR activity measurement in RDE

Identical catalyst ink formulation and RDE setup was used for PRR measurements with the exception that the working electrode used was a glassy carbon RDE without a platinum ring. After the catalyst break-in procedure in N_2 saturated electrolyte, an aliquot of 30 % (v/v) H_2O_2 solution (Sigma Aldrich) was added to the electrolyte to give a concentration of 10 mM H_2O_2 in N_2 saturated 0.5 M H_2SO_4. PRR polarization curves were measured at 2 $mV \cdot s^{-1}$ starting from OCP then scanned from 0 to 1 V *vs*. RHE with a rotation speed of 900 RPM.

2.3. Catalase measurements

The measurements for the evaluation of the catalase-like activity were performed in a three-neck round-bottomed flask: one for the O_2 probe (NEOFOX –KIT PROBE from Ocean Optics) used to measure continuously in time the produced oxygen, one neck for the septum for the injection of H_2O_2, and the last one for the expansion chamber to allow constant pressure in the system. The catalytic tests were performed with 16.5 mL of buffer solution (i.e. sodium citrate 0.1 M pH 4.02, or PBS pH 2.4 or HCl/KCl pH 0.9) and 0.51 mL of a catalyst suspension made up of either 1 mg/mL $Fe_{0.5}$ or 1 mg/mL NC, in which 0.05 mg mL^{-1} of α-$ZnMoO_4$, $Zn_3(OH)_2(MoO_4)_2$, or other soluble salts ($ZnCl_2$ or Na_2MoO_4) was further added. The oxygen produced by the H_2O_2 disproportionation was removed from the head space of the flask (head space volume 51.4 mL), whereas the unreacted H_2O_2 remaining in solution was independently measured to verify the overall yield of the catalase-like reaction. The detection of H_2O_2 was carried out using a titanium oxysulfate solution (~ 5 % Ti basis, in H_2SO_4 27–31 %, Sigma-Aldrich), which forms a complex with H_2O_2 with a characteristic absorption peak at 409 nm. An optical absorbance vs concentration calibration curve in the range from 1.2 µM to 2 mM of H_2O_2 was used to quantify the H_2O_2 concentration remaining at the end of the catalytic tests.

2.4. Structural and morphological characterizations

2.4.1. X-ray diffraction measurements

X-ray diffraction patterns of the M-N-C materials and the Zn-molybdates were recorded using a PANalytical X'Pert Pro powder X-ray diffractometer equipped with a Cu Kα radiation source and 1-D strip detector in Bragg-Brentano focusing geometry. A receiving slit filter was used to remove Cu Kβ. Powder specimens were loaded into zero-background Si single crystal sample holders mounted on a spinning sample stage to improve particle statistics. A continuous scan rate of 1.5 °/min was used and intensity was averaged over a 0.05° step size.

2.4.2. ^{57}Fe Mössbauer spectroscopy measurement

The ^{57}Fe Mössbauer spectrum measured for the Fe-N-C prepared via a two-step synthesis in the present study was acquired in identical conditions to those applied in our earlier studies to measure the spectrum of $Fe_{0.5}$. The source was ^{57}Co in rhodium and the spectrometer was from Wissel (Germany). The spectrum was acquired in transmission mode. The velocity driver was operated in constant acceleration mode with a triangular velocity waveform. The velocity scale was calibrated at room temperature with the magnetically split sextet of a high-purity α-Fe foil. The measured spectrum was fitted to appropriate combinations of Lorentzian profiles representing quadrupole doublets, sextets by least-squares methods. The fittings were performed with unconstrained parameters (relative area, IS, QS, LW, H) for each spectral component. The fitted isomer shift (IS) values are reported relative to α-Fe at room temperature. Fe-N-C powder was mounted in a 2 cm^2 holder. Mössbauer measurements at 5 K were performed in a helium flow cryostat (SHI-850 Series from Janis, USA).

2.4.3. X-ray absorption spectroscopy

Fe K-edge X-ray absorption spectroscopy (XAS) was conducted in transmission mode on the Fe-N-C material at room temperature at the SAMBA beamline (Synchrotron SOLEIL). The beamline is equipped with a sagittally focusing Si 220 monochromator and two Pd-coated mirrors that were used to remove X-ray harmonics. The catalyst was pelletized as a disk of 10 mm diameter using Teflon powder (1 µm particle size) as a binder.

2.4.4. Scanning electron microscopy

The morphology of the Zn molybdate and Zn molybdenum oxide was investigated with SEM (Hitachi S-4800, Hitachi, Tokyo, Japan) operating at 2 kV. Zn molybdate samples were dispersed on electrically conductive adhesive tape followed by gold metallization to improve sample conductivity.

2.4.5. Nitrogen physisorption measurements

The Brunauer–Emmett–Teller (BET) surface area and pore volume of the Zn-molybdate and Zn molybdenum oxide were measured with N_2 sorption at 77 K using a Micromeritics ASAP 2020 instrument. Before the measurement, the samples were degassed at 200 °C for 12 h under vacuum.

2.4.6. XPS measurements

X-ray photoemission spectra were acquired in a custom build Ultra High Vacuum chamber with a base pressure of $5x10^{-10}$ mBar coupled with a non-monochromatized double-anode X ray source (Omicron DAR-400, Scienta-Omicron GmbH, Uppsala, Sweden), a hemispherical electron analyzer (Omicron EA-125, Scienta-Omicron GmbH, Uppsala, Sweden) and a 5-channeltron detection assembly. The electron analyzer had an acceptance angle of ±4° and the diameter of the analyzed area was 3mm. The spectra were collected with Al-kα radiation, for the high-resolution spectra was used 20 eV as pass energy, a step of 0.1 eV and a dwell time of 0.25 s.

3. Results and Discussion

3.1. Materials characterisation

α-$ZnMoO_4$ and $Zn_3(OH)_2(MoO_4)_2$ were first studied as peroxide scavengers. The α-$ZnMoO_4$ material was purchased from Sigma Aldrich (99.9 % pure) and used as received, while $Zn_3(OH)_2(MoO_4)_2$ was prepared from α-$ZnMoO_4$ by reacting it with a 30 wt% H_2O_2 aqueous solution at room temperature (see details in the Experimental Methods). The commercial α-$ZnMoO_4$ polymorph was phase pure, all X-ray diffraction (XRD) peaks matching those calculated for this structure (**Figure S1a**), while the prepared $Zn_3(OH)_2(MoO_4)_2$ contains a residual amount of α-$ZnMoO_4$ (**Figure S1b**). Their porosity was

measured with N_2 sorption (**Figure S1c**). The as-received α-$ZnMoO_4$ is almost non-porous, while $Zn_3(OH)_2(MoO_4)_2$ adsorbs a significant amount of N_2 across the entire range of P/P^0, implying the coexistence of some microporosity (some volume is already adsorbed at the lowest P/P^o value), and mainly mesoporosity. The BET surface area of $Zn_3(OH)_2(MoO_4)_2$ was estimated to be 44 $m^2 \cdot g^{-1}$. Scanning electron microscopy (SEM) also identified morphological differences between α-$ZnMoO_4$ and $Zn_3(OH)_2(MoO_4)_2$, α-$ZnMoO_4$ presenting 5-8 µm large cobblestone-resembling morphology with smooth outer surface, and $Zn_3(OH)_2(MoO_4)_2$ showing a fine lamellar structure about 60 nm thick and from 300 nm up to 3-5 µm in lateral size (**Figure S2**).

Then, we investigated the effect of α-$ZnMoO_4$ or $Zn_3(OH)_2(MoO_4)_2$ on the ORR selectivity of Fe-N-C, Co-N-C and Cr-N-C materials with a RRDE setup. Except for the nature of the metal, the three M-N-C materials were prepared similarly *via* a two-step pyrolysis approach, the first pyrolysis leading to the formation of N-C from ZIF-8 (Basolite® Z1200 from BASF), and the second pyrolysis leading to M-N-C after the addition of metal chloride onto N-C (see details in the Experimental Methods). These three M-N-C materials were characterised by XRD (**Figure 1a**) and, for Fe-N-C, also with X-ray absorption spectroscopy and ^{57}Fe Mössbauer spectroscopy (**Figure 1b-c**). The XRD patterns only show broad peaks associated with the presence of small and/or amorphous graphite crystallites, suggesting the presence of metal as atomically dispersed M-N_x moieties and/or as ultra-small clusters. The Fourier-transform of the Extended X-ray Absorption Fine Structure (FT-EXAFS) at the Fe K-edge prior to phase correction shows a main peak at *ca* 1.5 Å for Fe-N-C, that can be assigned to Fe-N or Fe-O contribution from FeN_x sites, and a minor peak at *ca* 2.5 Å that can be assigned either to Fe-C interaction from the second coordination sphere of Fe in FeN_x sites, or to Fe-Fe interaction in iron oxides. The FT-EXAFS of Fe-N-C is comparable to that of $Fe_{0.5}$ (**Figure 1b**), the latter being an internal reference of our laboratory and for which the fitting of the FT-EXAFS previously revealed the sole presence of Fe-N_4 sites, with an axial oxygen ligand. [34] The FT-EXAFS results on Fe-N-C are supported by ^{57}Fe Mössbauer spectroscopy (**Figure 1c** and **Table S1**), identifying two doublets D1 and D2 that are ubiquitous in atomically-dispersed Fe-N-C catalysts, [34-36] and recently identified by us to be high-spin Fe(III)-N_4 sites (with an

axial oxygen ligand atop the Fe cation) and low- or medium-spin Fe(II)-N_4 sites, respectively. [37,38] The ^{57}Fe Mössbauer spectrum was fitted with a third spectral component, namely a broad singlet. The latter may be assigned to magnetically disordered Fe clusters, and its isomer shift of ~0.47 mm s^{-1} suggests some oxidized form of Fe clusters.

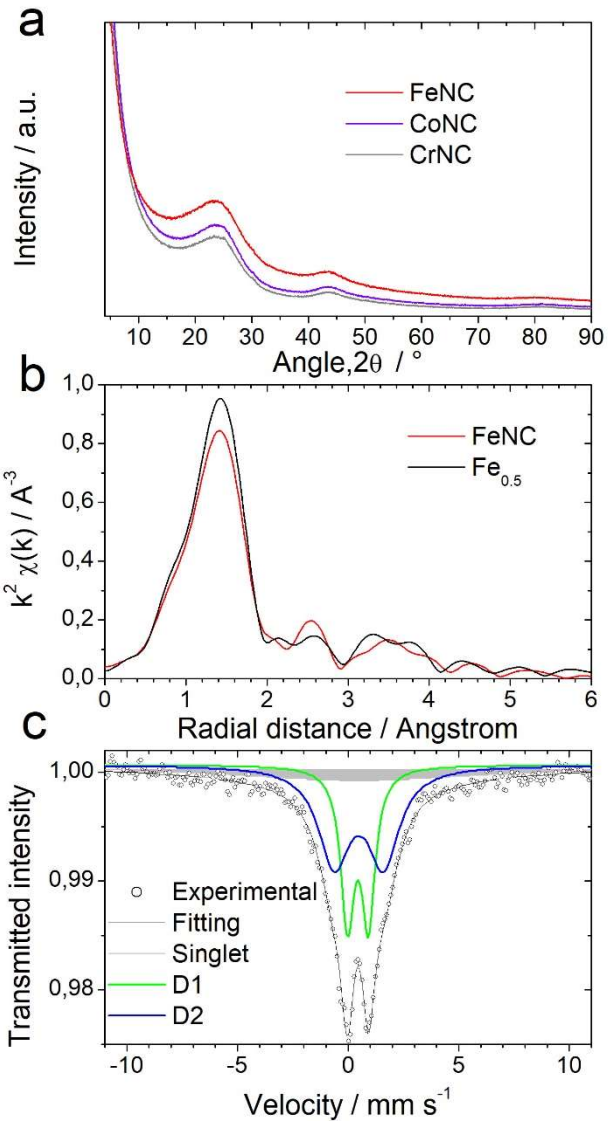

Figure 1. Structural characterisation of M-N-C materials. a) XRD patterns of Fe-N-C, Co-N-C, and Cr-N-C, b) FT-EXAFS of Fe-N-C and $Fe_{0.5}$, c) ^{57}Fe Mössbauer spectrum of Fe-N-C. The Mössbauer spectrum was acquired at 5 K and the velocity scale was calibrated versus a metallic iron foil.

3.2. Activity and selectivity towards ORR

The peroxide yield and Faradaic ORR current density were measured as a function of the electrochemical potential in a RRDE setup for each M-N-C catalyst, and then for each M-N-C material with the addition of α-$ZnMoO_4$ or $Zn_3(OH)_2(MoO_4)_2$ in a mass ratio for $ZnMoO_x$/M-N-C of 1/10 at the ink preparation stage. The results for α-$ZnMoO_4$/Fe-N-C and $Zn_3(OH)_2(MoO_4)_2$/Fe-N-C show that both zinc molybdenum compounds contribute to the decrease of the peroxide yield across the entire potential range compared to Fe-N-C alone (**Figure 2a** and **Figure 2b**, respectively). The ORR activities of the bifunctional $ZnMoO_x$/Fe-N-C layers are identical to that of Fe-N-C alone, as shown by superimposed polarisation curves at E > 0.8 V, indicating that the addition of α-$ZnMoO_4$ or $Zn_3(OH)_2(MoO_4)_2$ did not block Fe-based active sites. This is further supported by the cyclic voltammograms (CV) acquired in N_2-saturated electrolyte for the Fe-N-C layer and $Zn_3(OH)_2(MoO_4)$/Fe-N-C bifunctional layer (**Figure S3**). The signals are generally superimposed, indicating similar electrochemical surface area of carbon. However, for $Zn_3(OH)_2(MoO_4)_2$/Fe-N-C, an additional reduction peak is seen at *ca* 0.37 V *vs*. RHE and the oxidation peak at 0.62-0.64 V *vs.* RHE has a higher intensity compared to Fe-N-C, and its position on the potential scale is negatively shifted by *ca* 30 mV. This can be interpreted as a redox peak contribution from $Zn_3(OH)_2(MoO_4)_2$, with broad separation between its reduction and oxidation peaks. The ORR polarisation curve of $Zn_3(OH)_2(MoO_4)_2$/Fe-N-C shows a higher and better-defined diffusion-limited current density than Fe-N-C (**Figure 2a**), while the polarisation curve of α-$ZnMoO_4$/Fe-N-C is superimposed with that of Fe-N-C across the entire potential range (**Figure 2b**). Since the peroxide yield on Fe-N-C is at maximum *ca* 6 % only (at 0.0 V *vs*. RHE), the maximum increase in current density that might be observed in the diffusion-limited region is only *ca* 3% if no peroxide at all were produced with $ZnMoO_x$/Fe-N-C layers. However, the gain in current density for $Zn_3(OH)_2(MoO_4)_2$/Fe-N-C *vs.* Fe-N-C at E < 0.7 V vs. RHE significantly exceeds this value (*ca* 7 and 21% higher current density at 0.0 and 0.5 V *vs*. RHE, respectively). Therefore, the higher current density observed at low potentials for $Zn_3(OH)_2(MoO_4)_2$/Fe-N-C *vs.* Fe-N-C is the combined result of decreased peroxide yield and improved O_2 mass-transport or layer uniformity in the

$Zn_3(OH)_2(MoO_4)_2$/Fe-N-C layer. In contrast, the nearly superimposed polarisation curves for α-$ZnMoO_4$/Fe-N-C and Fe-N-C (**Figure 2b**) suggest that the addition of α-$ZnMoO_4$ did not improve O_2 mass-transport nor layer uniformity. This difference can be assigned to the contrasted morphologies of α-$ZnMoO_4$ and $Zn_3(OH)_2(MoO_4)_2$ that were described previously.

On the basis of slightly further decreased peroxide yield with $Zn_3(OH)_2(MoO_4)_2$ compared with α-$ZnMoO_4$ and the peroxide-induced phase transformation from α-$ZnMoO_4$ to $Zn_3(OH)_2(MoO_4)_2$ (used to prepare $Zn_3(OH)_2(MoO_4)_2$, but which may transform also α-$ZnMoO_4$ into $Zn_3(OH)_2(MoO_4)_2$ in *operando*, as a result of H_2O_2 production during ORR), we selected $Zn_3(OH)_2(MoO_4)_2$ to investigate its effect on other M-N-C materials. The results for $Zn_3(OH)_2(MoO_4)_2$/Co-N-C and $Zn_3(OH)_2(MoO_4)_2$/Cr-N-C (**Figure 2c** and **Figure 2d**, respectively) show strongly reduced peroxide yields compared to the measurements with Co-N-C and Cr-N-C. The trends are similar to those observed with the $Zn_3(OH)_2(MoO_4)_2$/Fe-N-C bifunctional layer, with a reduced peroxide yield across the entire potential range, similar ORR activity at 0.8 V *vs*. RHE with and without Zn molybdenum oxide, and increased current density with $Zn_3(OH)_2(MoO_4)_2$ in the layer at E < 0.70-0.75 V *vs*. RHE. The positive effect of $Zn_3(OH)_2(MoO_4)_2$ addition is dramatic with Co-N-C, due to the high peroxide yield with that catalyst alone (12-19 % at E < 0.7 V *vs*. RHE). As for $Zn_3(OH)_2(MoO_4)_2$/Fe-N-C, the increase in current density with $Zn_3(OH)_2(MoO_4)_2$ in the diffusion-limited region exceeds the value that would be expected from the decreased peroxide yield. Even for Co-N-C, the maximum increase in current density at low potential expected from peroxide yield measurements would be *ca* 11 %. However, 35 and 63 % increase in current density is experimentally observed at 0.0 and 0.5 V *vs.* RHE, respectively. Therefore, it may be concluded that the addition of $Zn_3(OH)_2(MoO_4)_2$ in the catalytic layers of Fe-N-C, Co-N-C and Cr-N-C results in i) decreased peroxide yield and ii) improved layer uniformity or O_2 mass-transport. In summary, the results show that the addition of α-$ZnMoO_4$ and $Zn_3(OH)_2(MoO_4)_2$ strongly reduces the peroxide yield of M-N-C catalysts without negatively affecting the ORR activity of the layers and that this effect is applicable to M-N-C catalysts with different active metal centers (Fe, Co, Cr).

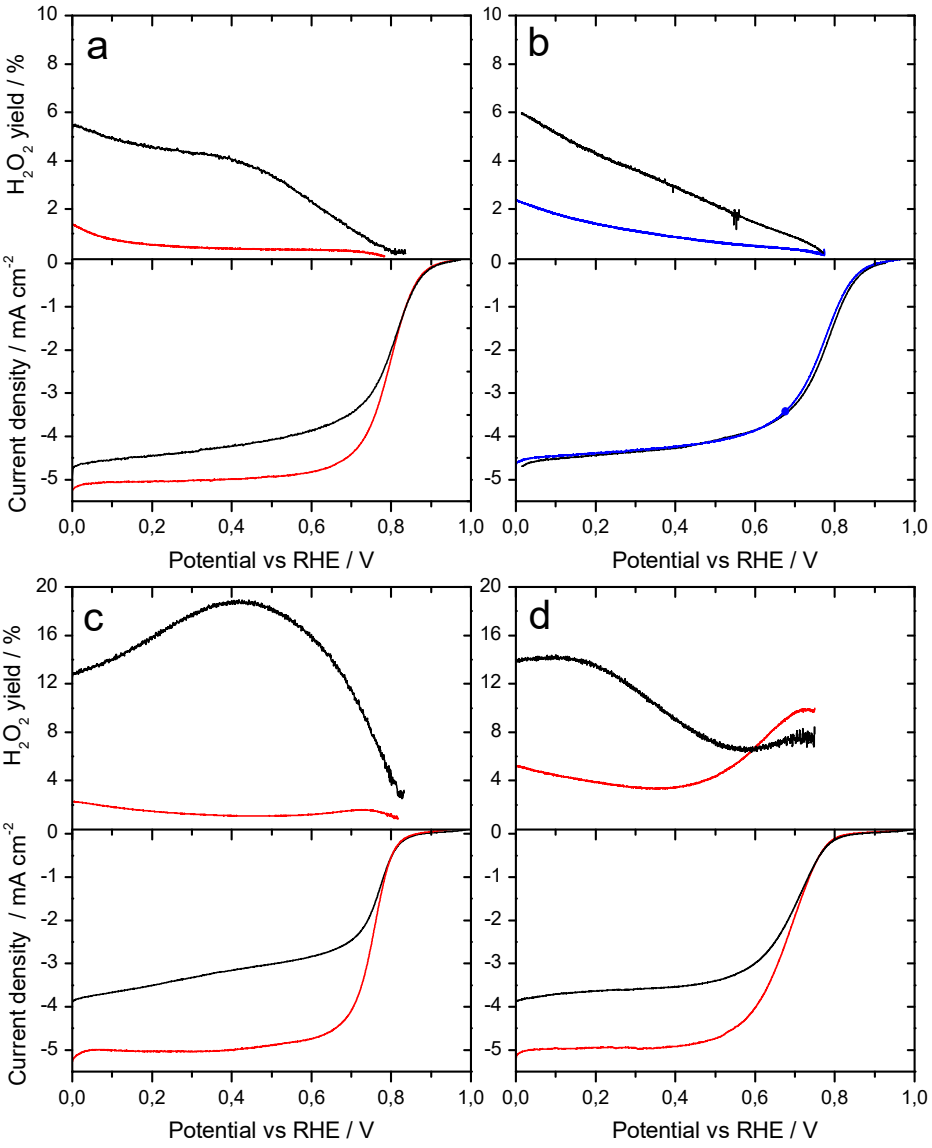

Figure 2. ORR activity and selectivity of M-N-C catalyst and $ZnMoO_x$/M-N-C bifunctional catalytic layers. Peroxide yield and ORR polarisation curve for a) Fe-N-C (black) and $Zn_3(OH)_2(MoO_4)_2$/Fe-N-C (red), b) Fe-N-C (black) and α-$ZnMoO_4$/Fe-N-C (blue), c) Co-N-C (black) and $Zn_3(OH)_2(MoO_4)_2$/Co-N-C (red), d) Cr-N-C (black) and $Zn_3(OH)_2(MoO_4)_2$/Cr-N-C (red). The M-N-C and $ZnMoO_x$ loadings are 800 and 80 $\mu g \cdot cm^{-2}$, respectively. The electrolyte is 0.5 M H_2SO_4, scan rate 2 $mV \cdot s^{-1}$ and rotation rate 1600 rpm. Note: non-identical curves for Fe-N-C in a) and b) are due to the fact that two different batches of Fe-N-C were used.

3.3. Reactivity of $ZnMoO_x$ and bifunctional layers towards hydrogen peroxide

Then we designed experiments to identify the underlying mechanism through which $Zn_3(OH)_2(MoO_4)_2$ and α-$ZnMoO_4$ decrease the peroxide yield during ORR catalysis with M-N-C catalysts. For this purpose, we used a reference Fe-N-C catalyst previously developed at our laboratory and that does not contain any Fe particles (or in such low amount that they cannot be detected by the present techniques). [34] The catalyst is labelled $Fe_{0.5}$, as in our previous studies. [8, 34, 37, 38] We first investigated the activity of $Zn_3(OH)_2(MoO_4)_2$ for the hydrogen peroxide reduction reaction (PRR). A layer of $Zn_3(OH)_2(MoO_4)_2$ and Ketjenblack (a high surface area carbon black) with a mass ratio $Zn_3(OH)_2(MoO_4)_2$/carbon of 1/4 shows no PRR activity down to *ca* 0.3 V *vs*. RHE (**Figure S4**, black curve). Under the assumption that PRR activity may arise from a synergy between M-N-C and $Zn_3(OH)_2(MoO_4)_2$, we then measured the PRR activity of $Zn_3(OH)_2(MoO_4)_2/Fe_{0.5}$ and α-$ZnMoO_4/Fe_{0.5}$ layers (1/10 mass ratio) and compared it to that of $Fe_{0.5}$. The results show strongly enhanced PRR activity for the bifunctional layers with similar enhancement for $Zn_3(OH)_2(MoO_4)_2/Fe_{0.5}$ and α-$ZnMoO_4/Fe_{0.5}$ layers relative to $Fe_{0.5}$ (**Figure 3**). The results explain the increased four-electron selectivity for the bifunctional layers reported in **Figure 2**. However, the positive effects of $Zn_3(OH)_2(MoO_4)_2$ and α-$ZnMoO_4$ in increasing the PRR activity are similar (**Figure 3**), which is in slight contrast with the stronger reduction in % H_2O_2 with $Zn_3(OH)_2(MoO_4)_2$ than with α-$ZnMoO_4$ seen in **Figure 2**. The decreased % H_2O_2 with bifunctional layers in **Figure 2** is seen at E < 0.8 V *vs.* RHE, in line with the onset potential for PRR at *ca* 0.84 V vs. RHE seen in **Figure 3**. A control experiment with $Zn_3(OH)_2(MoO_4)_2$ mixed with an iron-free N-doped carbon prepared otherwise similarly as $Fe_{0.5}$ (labelled as N-C) shows that the synergy at play is between $Zn_3(OH)_2(MoO_4)_2$ and the Fe-N_4 centers, not between $Zn_3(OH)_2(MoO_4)_2$ and metal-free nitrogen moieties or Zn-N_4 moieties present in N-C (dotted red curve in **Figure 3**). Also supporting this, the %H_2O_2 produced during ORR on N-C is high, and unmodified by the addition of $Zn_3(OH)_2(MoO_4)_2$ (**Figure S5**). Note however that the maximum current density for HPRR reached at 0.0 V vs RHE by the $Zn_3(OH)_2(MoO_4)_2/Fe_{0.5}$ layers is only 5.0-5.5 mA cm^{-2} (**Figure 3**), which is much less than the expected diffusion-limited current density at 10 mM H_2O_2 and 1600 rpm (*ca* 15 mA cm^{-2} expected, based on the

ca 2.2 mA cm^{-2} HPRR diffusion limited current density reported at 1600 rpm and with 1.3 mM H_2O_2 in pH 1 solution with Pt/C, [39]). Previous works studying HPRR on Fe-N-C materials reported a similar observation, with HPRR polarization curves that only slightly depend on rotation rate, and with maximum current density well below the one expected for two-electron HPRR according to the Levich equation. [39-41] This indicates that the HPRR on such materials is limited by a chemical step, and that the limitation is mitigated by adding $Zn_3(OH)_2(MoO_4)_2$ to $Fe_{0.5}$.

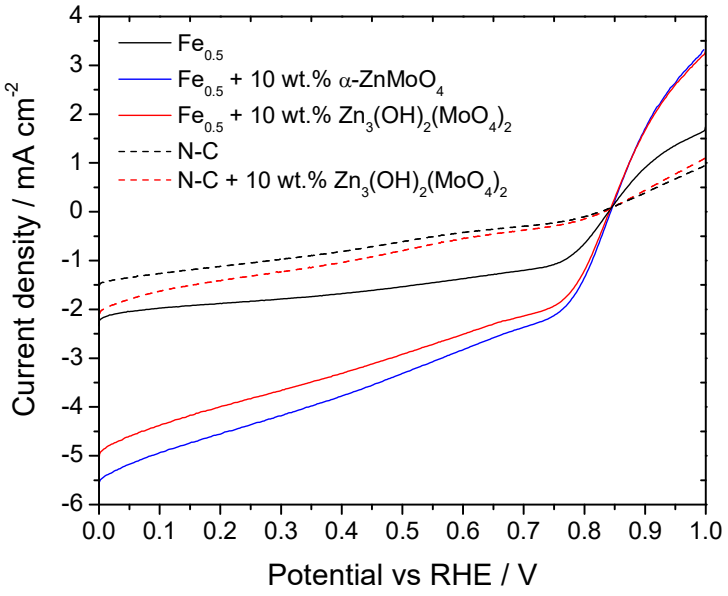

Figure 3. Activity toward H_2O_2 electroreduction of α-$ZnMoO_4$/$Fe_{0.5}$, $Zn_3(OH)_2(MoO_4)_2$/$Fe_{0.5}$, $Zn_3(OH)_2(MoO_4)_2$/N-C, $Fe_{0.5}$ and N-C. H_2O_2 electroreduction was measured in 10 mM H_2O_2 in 0.5 M H_2SO_4 electrolyte at 1600 rpm with a scan rate of 2 mV s^{-1}. The loading of $Fe_{0.5}$ and $ZnMoO_x$ was 800 and 80 µg·cm^{-2}, respectively.

To investigate the suspected activity of $ZnMoO_4$ or $Zn_3(OH)_2(MoO_4)_2$ in catalyzing heterogeneous reactions with hydrogen peroxide, we also applied methods previously developed for investigating the catalase-like activity of nanozymes, [42,43]. Nanozymes are generally defined *as* inorganic nanoparticle with the ability to mimick the catalytic activity of natural biomolecules. [44] The activity of the enzyme catalase or a nanozyme enzyme-mimetic is therefore the ability to accelerate the

disproportionation of H_2O_2 into O_2 and water, without the need for an electron donor. The catalase-like activity of $Zn_3(OH)_2(MoO_4)_2$ and α-$ZnMoO_4$ was investigated in the presence of N-C or $Fe_{0.5}$ by measuring the rate of O_2 evolved from H_2O_2 as a function of time (see Methods). Control experiments were also performed with N-C or $Fe_{0.5}$ alone. For each material (or combination), the O_2 evolution rate was measured for four different H_2O_2 concentrations (3, 15, 30, 60 mM). The plots for oxygen evolution at all four concentrations are shown for N-C, $Fe_{0.5}$, $Zn_3(OH)_2(MoO_4)_2$/N-C and α-$ZnMoO_4$/$Fe_{0.5}$ in **Figure S6**, and for $Zn_3(OH)_2(MoO_4)_2$/$Fe_{0.5}$ in **Figure 4a**. For catalase-like activity tests, the $ZnMoO_x$ content was always kept fixed at 5 wt % relative to $Fe_{0.5}$ or N-C. The O_2 evolution vs. time curves can be compared for all materials or material combinations at the fixed concentration of 60 mM H_2O_2, as shown in **Figure 4b**. At short times, the trend of the O_2 evolution rate for the different materials or material combinations is $Zn_3(OH)_2(MoO_4)_2$/$Fe_{0.5}$ $\geq$ α-$ZnMoO_4$/$Fe_{0.5}$ >> $Fe_{0.5}$ >> $Zn_3(OH)_2(MoO_4)_2$/N-C > N-C $\geq$ $Zn_3(OH)_2(MoO_4)_2$. This trend is in line with the results of peroxide yield observed in RRDE setup (**Figure 2**). While the coexistence in solution of $Zn_3(OH)_2(MoO_4)_2$ and $Fe_{0.5}$ initially leads to the highest O_2 evolution rate, a higher conversion rate of peroxide into O_2 is observed after around 2 h with the combination of α-$ZnMoO_4$ and $Fe_{0.5}$, and a higher saturation conversion is also achieved after 3 h (96% vs. 85%, **Figure 4b**). However, at lower peroxide concentrations, both $Zn_3(OH)_2(MoO_4)_2$/$Fe_{0.5}$ and α-$ZnMoO_4$/$Fe_{0.5}$ catalyze an almost complete conversion of H_2O_2 to O_2 within 2 h (94-97%) with initial H_2O_2 concentrations of 3 and 15 mM (**Table S2**). This suggests that the decomposition channel is selective. The duration required to completely remove H_2O_2 may however allow some material degradation to take place in parallel.

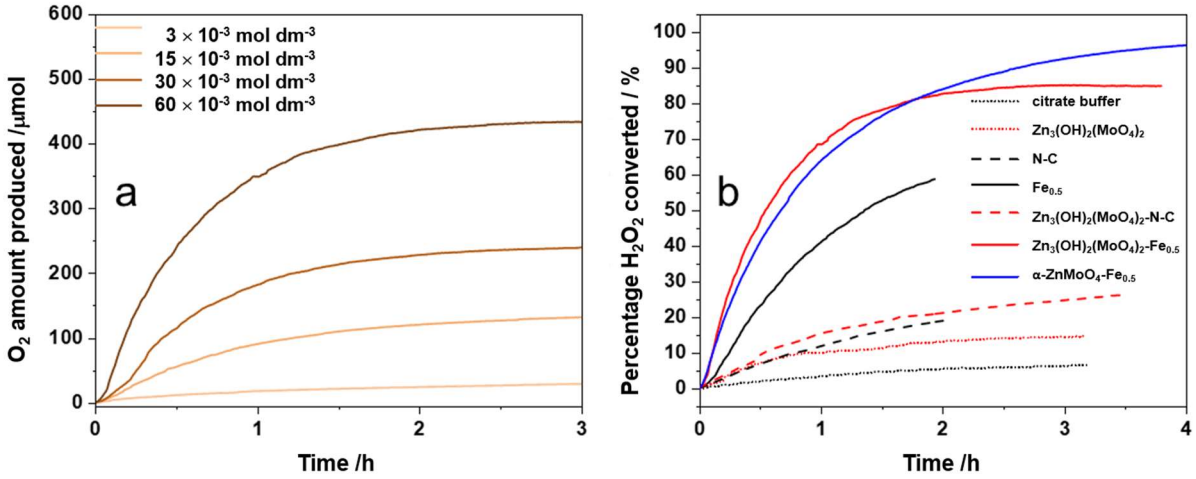

Figure 4. a) Produced O_2 amount versus time for $Zn_3(OH)_2(MoO_4)_2/Fe_{0.5}$ with different concentrations of H_2O_2. b) Conversion of H_2O_2 into O_2 on the different materials at pH 4, (sodium citrate buffer solution 0.1 M) starting from the same initial concentration of H_2O_2 (60 mM).

Notably, the catalytic activities observed with iron-free materials or material combinations, *i.e.* $Zn_3(OH)_2(MoO_4)_2$, N-C and $Zn_3(OH)_2(MoO_4)_2$/N-C are modest, all iron-free combinations showing similar and low initial reaction rates. This suggests that iron species might be the catalytic centers, and that a synergy between zinc molybdates and FeN_x centers further accelerates the peroxide disproportionation by Fe-based sites. In contrast, no synergistic effects can be observed between the zinc molybdate or Zn molybdenum oxide and the nitrogen moieties in N-C, also in line with the electrochemical investigation in RRDE.

We then attempted to analyze the reaction profiles of peroxide heterogeneous disproportionation within the theoretical framework of a Michaelis-Menten kinetic model, which is commonly used for enzymes and nanozymes. However only in the case of $Zn_3(OH)_2(MoO_4)_2/Fe_{0.5}$, α-$ZnMoO_4/Fe_{0.5}$, and $Fe_{0.5}$ were straight lines observed in the Lineweaver–Burk double reciprocal plots (**Figure S7**). The results of the Michaelis-Menten analysis for $Fe_{0.5}$, $Zn_3(OH)_2(MoO_4)_2/Fe_{0.5}$ and α-$ZnMoO_4/Fe_{0.5}$ are reported in **Table S3**. The data clearly confirm the hypothesis that the combination of zinc molybdate or zinc

molybdenum oxide with the iron catalyst results in an increase in the catalase-like activity that is higher than the simple sum of the single catalytic activities. The general trend deduced from the direct comparison of the reaction profiles is quantitatively confirmed, with $Zn_3(OH)_2(MoO_4)_2/Fe_{0.5}$ being more active than α-$ZnMoO_4$/ $Fe_{0.5}$, especially in terms of V_{max}, and both of them being more active than $Fe_{0.5}$. Notably, the trend of the K_m values indicates that H_2O_2 has higher affinity for the iron centers than the $ZnMoO_x$ materials. Overall, the catalytic performance of $Zn_3(OH)_2(MoO_4)_2/Fe_{0.5}$ is very good compared with that of other transition-metal-based nanozymes developed to mimic catalase (**Table S4**), such as ferritin-platinum nanoparticles, [45] graphene Fe_2O_3 nanohybrids, [43] Co_3O_4, [46-47] and capped Fe_2O_3/Fe_3O_4 nanoparticles. [48] Given the intended application of $ZnMoO_x$/Fe-N-C materials in the acidic environment of PEMFC, a series of experiments was performed in more acidic buffered solutions, *i.e.* phosphate buffer solution (PBS) with a pH of 2.42, and KCl/HCl with a pH of 0.9 (**Figure S8**). As expected, the catalytic activity is strongly suppressed as the pH is reduced, although peroxide disproportionation is still clearly detectable for 5 wt% $Zn_3(OH)_2(MoO_4)_2/Fe_{0.5}$, whereas other groups previously reported that other nanozymes in similar conditions are completely inactive. [45]

Further insights on the mechanism of hydrogen peroxide decomposition were obtained from XPS measurements (**Figure 5**). The $Zn_3(OH)_2(MoO_4)_2$ and its physical mixture with either $Fe_{0.5}$ or N-C were suspended in 60 mM H_2O_2 solution buffered to pH 4 by citrate, incubated for 30 min and then drop cast on a solid support and dried under vacuum. The resulting dried films were investigated by XPS and the spectra were compared to the data acquired on samples that were not exposed to H_2O_2. For all samples, the Zn $2p_{3/2}$ photoemission line did not undergo any apparent change after the exposure to H_2O_2, showing a single component peak centered at about 1022 eV, which corresponds to Zn^{2+}. On the other hand, the Mo 3d photoemission line exhibits an interesting behavior. In the pristine $Zn_3(OH)_2(MoO_4)_2$ sample, the Mo 3d photoemission line consists of a single doublet component with the Mo $3d_{5/2}$ peak centered at 232.2 eV, which can be ascribed to Mo^{6+} ions. After the incubation with H_2O_2 an additional component can be identified at 230 eV, which indicates the formation of Mo^{4+} species. [49, 50] Whereas in the $Zn_3(OH)_2(MoO_4)_2$ sample such Mo^{4+} represents only 22 % of the whole

Mo species after H_2O_2 incubation, in the physical mixture of $Zn_3(OH)_2(MoO_4)_2$ with $Fe_{0.5}$, it is possible to observe the complete disappearance of Mo^{6+} and its complete conversion to Mo^{4+} after the same H_2O_2 incubation. Moreover, when $Zn_3(OH)_2(MoO_4)_2$ is mixed with N-C, no reduction of molybdenum is observed after H_2O_2 incubation, ruling out that the reduction can be due to a direct solid-state reaction between the metal oxide and the carbon support. The body of these spectroscopic data therefore indicates a strong synergy between iron species and the metal oxide. Iron is key to activate the H_2O_2 molecule, which therefore is able to reduce Mo^{6+} to Mo^{4+}. The ability of some Fe-N_4 sites in $Fe_{0.5}$ to reversibly change oxidation state between +III and +II may also play a role in the reduction of Mo. [51] These effects explain why the catalytic activity towards the decomposition of H_2O_2 is poor on the zinc molybdenum oxide alone (*i.e.* H_2O_2 is not activated), while is boosted in the $Zn_3(OH)_2(MoO_4)_2/Fe_{0.5}$ composite system (*i.e.* the redox active Mo species may sustain a catalytic cycle as promoters in synergy with FeN_x sites).

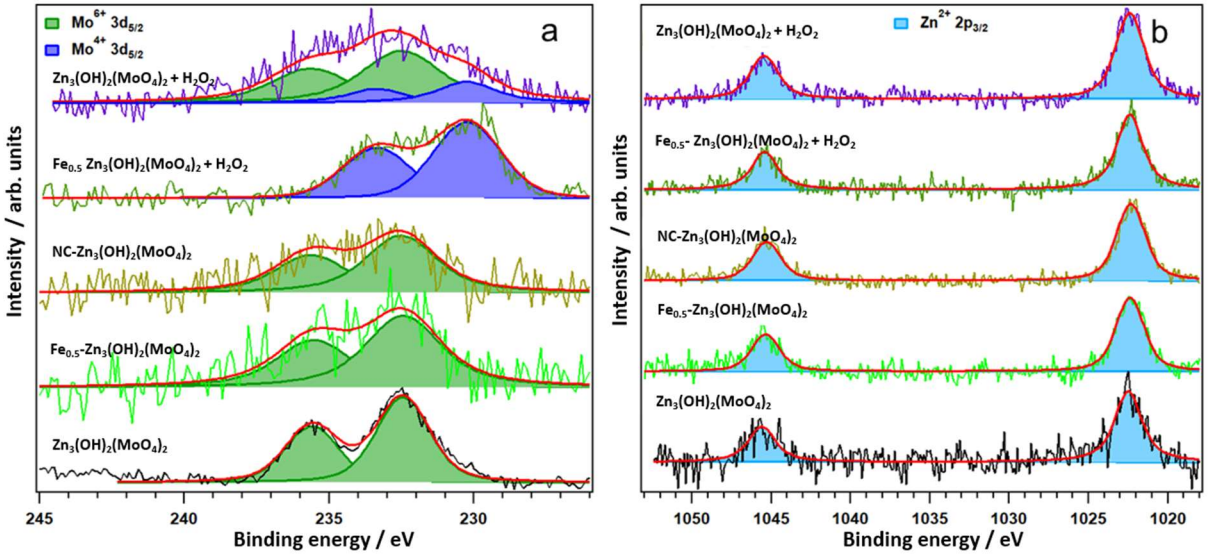

Figure 5. Mo 3d (a) and Zn 2p (b) photoemission spectra acquired on the different materials or material combinations after incubation in citrate buffer solution with or without H_2O_2 (concentration 60 mM).

Given the application of these catalysts at low pH conditions (pH ~ 1) in PEMFC, we explored the possibility that $ZnMoO_4$ or $Zn_3(OH)_2(MoO_4)_2$ can partially dissolve and provide ions that can act as

homogeneous catalysts. We therefore evaluated the catalase-like activity of soluble salts (0.05 mg/mL) of Zn^{2+} ($ZnCl_2$) and MoO_4^{2-} (Na_2MoO_4), either with or without $Fe_{0.5}$ suspended in solution, in order to identify the possible existence of synergistic effects between $Fe_{0.5}$ and these ions. The kinetic profiles of O_2 evolution as a function of time clearly indicate the molybdates anions have *per se* a low activity, whereas Zn^{2+} cations are significantly active with an overall performance for $ZnCl_2$ alone that is comparable to that of $Fe_{0.5}$ (**Figure S9**). As in the previous cases, strong synergistic effects are revealed when $Fe_{0.5}$ and the metal salts are simultaneously present in solution (**Figure S9**), and this is particularly visible in the case of i) Na_2MoO_4 and $Fe_{0.5}$ combination, and ii) $ZnCl_2$ and $Fe_{0.5}$ combination, which achieve a higher performance than $Zn_3(OH)_2(MoO_4)_2/Fe_{0.5}$. This agrees with the XPS data, indicating that only in the presence of $Fe_{0.5}$, the molybdate phase was activated and able to react with H_2O_2. These data help also to explain why systems obtained by a physical mixture of micrometric nanoparticles unexpectedly exhibit such a strong (electro)catalytic synergy, which on the other hand implies a nanoscale interaction. In fact, we can assume that the high activity observed in the heterogeneous $ZnMoO_x$/M-N-C composites results from the interaction of dissolved ions, either Zn(II) or MoO_4^{2-}, with Fe-N_x centers. Such a mechanism is particularly appealing because it may activate Fe-N_x catalytic centers within micro- and meso- pores that normally would not have contact with large $ZnMoO_x$ particles.

3.4. Accelerated stress tests in RDE setup

Based on the foregoing results and identification of $Zn_3(OH)_2(MoO_4)_2$ as a promising peroxide scavenger working in synergy with Fe-N_x sites to decrease the peroxide yield during ORR, we performed load-cycling accelerated stress tests (AST) in RRDE setup on the bifunctional layer of $Zn_3(OH)_2(MoO_4)_2/Fe_{0.5}$ and compared the results to those with $Fe_{0.5}$ alone. **Figure 6** shows comparable increase in peroxide yield at end-of-test (EoT) relative to beginning-of-test (BoT) for $Fe_{0.5}$ (**Figure 6a**) and $Zn_3(OH)_2(MoO_4)_2/Fe_{0.5}$ (**Figure 6c**), and also comparable decrease in ORR activity (**Figure 6b** and **6d**). The electrochemical potential at -1 mA cm^{-2} shifted negatively by 36 mV for $Fe_{0.5}$ and only 28 mV

for $Zn_3(OH)_2(MoO_4)_2/Fe_{0.5}$. The data therefore suggests a partial stabilisation of the ORR activity of $Fe_{0.5}$ by $Zn_3(OH)_2(MoO_4)_2$ in acidic medium. The incomplete stabilisation may be due to the low concentration in the catalytic layer of the ions resulting from $Zn_3(OH)_2(MoO_4)_2$ dissolution, or to a still insufficient rate of peroxide scavenging. The peroxide produced during ORR may undergo three main routes: a) removal from the catalytic layer by diffusion/convection, b) reaction with Fe-N_x sites leading to formation of ROS, c) reaction with $Zn_3(OH)_2(MoO_4)_2$ modified Fe-N_x sites, leading to peroxide disproportionation or electroreduction. For an efficient protection of Fe-N_x sites, the rate of the route c) should be higher than route b), which is likely not yet achieved with the present systems. Future studies will be needed to further improve our fundamental understanding of the synergy between α-$ZnMoO_4$ or $Zn_3(OH)_2(MoO_4)_2$ or its constituting metal ions and Metal-N_x sites, and practical approaches must be developed to efficiently utilize this effect in catalytic layers, especially in the PEMFC environment.

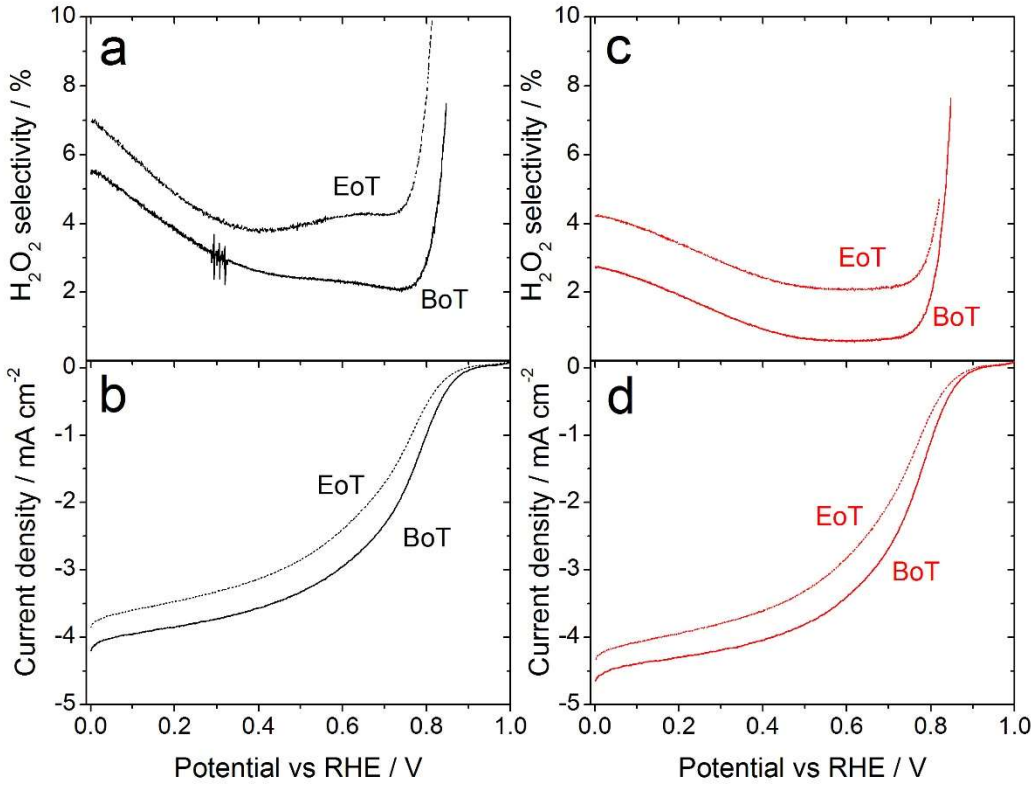

Figure 6. Stability of $Zn_3(OH)_2(MoO_4)_2$/$Fe_{0.5}$ bifunctional catalytic layer compared to $Fe_{0.5}$. a) Peroxide yield at BoT and EoT for $Fe_{0.5}$ **;** b) ORR polarisation curve at BoT and EoT for $Fe_{0.5}$ **;** c) Peroxide yield at BoT and EoT for $Zn_3(OH)_2(MoO_4)_2/Fe_{0.5}$ **;** d) ORR polarisation curve at BoT and EoT for $Zn_3(OH)_2(MoO_4)_2/Fe_{0.5}$. The solid and dashed curves correspond to BoT and EoT results, respectively. The $Fe_{0.5}$ and $Zn_3(OH)_2(MoO_4)_2$ loadings are 800 and 80 µg·cm^{-2}, respectively. Electrolyte is 0.5 M H_2SO_4, scan rate 2 mV·s^{-1} and rotation rate 1600 rpm for ORR polarisation curve acquisition. The AST consisted of 10,000 cycles between 0.6 and 0.925 V *vs.* RHE in O_2-saturated electrolyte, at a scan rate of 100 mV s^{-1}.

4. Conclusions

The addition of α-$ZnMoO_4$ or $Zn_3(OH)_2(MoO_4)_2$ to M-N-C catalysts was shown to improve the selectivity toward the four-electron reaction path in the ORR in acidic conditions. RRDE measurements suggest that both $ZnMnO_x$ materials, when combined with M-N-C catalysts exhibit excellent electrocatalytic peroxide reduction activity, confirming their potential to improve cathode layer durability by keeping the H_2O_2 and ROS concentration low. The high activity in H_2O_2 conversion was also confirmed by a series of catalase-like assays. The systematic investigation of different combinations of materials and model compounds allowed us to conclude that the FeN_x sites are the active catalase-like sites, but that their efficiency in significantly improved in the presence of $ZnMoO_x$. The study of the catalase-like activity of soluble metal salts, such as $ZnCl_2$ and Na_2MoO_4, which represent the homogenous catalyst counterparts of $ZnMoO_x$, suggest that these metal ions when leached from $ZnMoO_4$ and $Zn_3(OH)_2(MoO_4)_2$ particles at low pH conditions can be responsible for the synergistic interactions between $ZnMoO_x$ and FeN_x sites. Despite the excellent activity in both the chemical disproportionation and the electrochemical reduction of hydrogen peroxide, the results of accelerated stress tests in O_2-saturated acidic conditions showed only a modest improvement in the durability of catalytic layers comprising a Fe-N-C catalyst and $Zn_3(OH)_2(MoO_4)_2$. This could be explained by the still insufficiently effective mixing between the M-N-C layer and the zinc molybdate or by the need for even faster abatement of the local H_2O_2 concentration in order to fully suppress the possible formation of other ROS.

Acknowledgements

This work was funded by the Fuel Cells and Hydrogen 2 Joint Undertaking (now the Clean Hydrogen Joint Undertaking) under grant agreement no. 779366 (CRESCENDO project). This Joint Undertaking receives support from the European Union's Horizon 2020 research and innovation program, Hydrogen Europe and Hydrogen Europe Research. We are grateful to Bernard Fraisse and Nicolas Bibent for help

with XRD measurements and analysis, to Nicolas Donzel for help with N_2 sorption measurements, and to Andrea Zitolo for help with XAS measurements.

Declaration of competing interest

The authors have no competing interests to declare.

References

1. L. Jiao, J. Li, L. LaRochelle Richard, Q. Sun, T. Stracensky, E. Liu, M. Sougrati, Z. Zhao, F. Yang, S. Zhong, H. Xu, S. Mukerjee, Y. Huang, D. A. Cullen, J. H. Park, M. Ferrandon, D. J. Myers, F. Jaouen, Q. Jia, Chemical vapour deposition of Fe-N-C oxygen reduction catalysts with full utilization of dense Fe-N_4 sites, Nature Mater. 20 (2021) 1385.

2. L. Osmieri, J. Park, D. A. Cullen, P. Zelenay, D. J. Myers, K. C. Neyerlin, Status and challenges for the application of platinum group metal-free catalysts in proton-exchange membrane fuel cells, Curr. Opinion in Electrochemistry 25 (2021) 100627.

3. A. Uddin, L. Dunsmore, H. Zhang, L. Hu, G. Wu, S. Litster, High power density platinum group metal-free cathodes for polymer electrolyte fuel cells, ACS Appl. Mater. Interf. 12 (2019) 2216.

4. A. Mehmood, M. Gong, F. Jaouen, A. Roy, A. Zitolo, A. Khan, M. Sougrati, M. Primbs, A. M. Bonastre, D. Fongalland, G. Drazic, P. Strasser, A. Kucernak, High loading of single atomic iron sites in pyrolysed Fe-NC oxygen reduction catalysts for proton exchange membrane fuel cells, Nature Catalysis 5 (2021) 311.

5. K. Kumar, P. Gairola, M. Lions, N. Ranjbar-Sahraie, M. Mermoux, L. Dubau, A. Zitolo, F. Jaouen, F. Maillard, Physical and chemical considerations for improving catalytic activity and stability of non-precious-metal oxygen reduction reaction catalysts, ACS Catal. 8, (2018) 11264.

6. K. Kumar, L. Dubau, M. Mermoux, J. Li, A. Zitolo, J. Nelayah, F. Jaouen, F. Maillard, On the influence of oxygen on the degradation of Fe-N-C catalysts, Angew. Chemie Int. Ed. 59 (2020) 3235.

7. L. Osmieri, D. A. Cullen, H. T. Chung, R. K. Ahluwalia, K. C. Neyerlin, Durability evaluation of a Fe-N-C catalyst in polymer electrolyte fuel cell environment via accelerated stress tests, Nano Energy 78 (2020) 105209.

8. C. H. Choi, H-K. Lim, M. W. Chung, G. Chon, N. Ranjbar-Sahraie, A. Altin, M-T. Sougrati, L. Stievano, H. S. Oh, E. S. Park, F. Luo, P. Strasser, G. Drazic, K. J. J. Mayrhofer, H. Kim, F. Jaouen, The Achille's

heel of iron-based catalysts during oxygen reduction in an acidic medium, Energy Environ. Sci. 11, (2018) 3176.

9. Z. Chen, S. Jiang, G. Kang, D. Nguyen, G. C. Schatz, R. P. Van Duyne, Operando characterization of iron phthalocyanine deactivation during oxygen reduction reaction using electrochemical tip-enhanced raman spectroscopy, J. Am. Chem. Soc. 141 (2019) 15684.

10. X. Xie, C. He, B. Li, Y. He, D. A. Cullen, E. C. Wegener, A. J. Kropf, U. Martinez, Y. Cheng, M. H. Engelhard, M. E. Bowden, M. Song, T. Lemmon, X. S. Li, Z. Nie, J. liu, D. J. Myers, P. Zelenay, G. Wang, G. Wu, V. Ramani, Y. Shao, Performance enhancement and degradation mechanism identification of a single-atom Co-N-C catalyst for proton exchange membrane fuel cells, Nature Catalysis 3 (2020) 1044.

11. J. Li, M. Chen, D.A. Cullen, S. Hwang, M. Wang, B. Li, K. Liu, S. Karakalos, M. Lucero, H. Zhang, C. Lei, H. Xu, G. E. Sterbinsky, Z. Feng, D. Su, K. L. More, G. Wang, Z. Wang, G. Wu, Atomically dispersed manganese catalysts for oxygen reduction in proton-exchange membrane fuel cells, Nature Catalysis 1 (2018) 939.

12. F. Luo, A. Roy, L. Silvioli, D. A. Cullen, A. Zitolo, M. T. Sougrati, I. Can Oguz, T. Mineva, D. Teschner, S. Wagner, J. Wen, F. Dionigi, U. I. Kramm, J. Rossmeisl, F. Jaouen, P. Strasser, P-block single-metal-site tin/nitrogen-doped Carbon Fuel Cell Cathode Catalyst for Oxygen Reduction Reaction, Nature Mater. 19 (2020) 1215.

13. H. Wei, X. Su, J. Liu, J. Tian, Z. Wang, K. Sun, Z. Rui, W. Yang, Z. Zou, A CeO_2 modified phenylenediamine-based Fe/N/C with enhanced durability/stability as non-precious metal catalyst for oxygen reduction reaction, Electrochem. Commun. 88 (2018) 19.

14. M. Strlic, J. Kolar, V. S. Selih, D. Kocar, B. Pihlar, A comparative study of several transition metals in Fenton-like reaction systems at circum-neutral pH, Acta Chim. Slov. 50 (2003) 619.

15. Y. Sun, L. Silvioli, N. Ranjbar Sahraie, W. Ju, J. Li, A. Zitolo, S. Li, A. Bagger, L. Arnason, X. Wang, T. Moeller, D. Bernsmeier, J. Rossmeisl, F. Jaouen, P. Strasser, Activity-selectivity trends in the electrochemical production of hydrogen peroxide over single-site metal-nitrogen-carbon catalysts, J. Am. Chem. Soc. 141 (2019) 12372.

16. A. K. Mechler, N. Ranjbar Sahraie, V. Armel, A. Zitolo, M. T. Sougrati, J. N. Schwämmlein, D. J. Jones, F. Jaouen, Stabilization of iron-based fuel cell catalysts by non-catalytic platinum, J. Electrochem. Soc. 165 (2018) F1084.

17. T. Kosmala, N. Bibent, M. T. Sougrati, G. Drazic, S. Agnoli, F. Jaouen, G. Granozzi, Stable, active, and methanol-tolerant PGM-free surfaces in an acidic medium: electron tunnelling at play in Pt/FeNC hybrid catalysts for direct methanol fuel cell cathodes, ACS Catal. 10 (2020) 7475.

18. A. Ostroverkh, V. Johanek, M. Dubau, P. Kus, I. Khalakhan, B. Smid, R. Fiala, M. Vaclavu, Y. Ostroverkh, V. Matolin, Optimization of ionomer-free ultra-low loading Pt catalyst for anode/cathode of PEMFC via magnetron sputtering, Int. J. Hydrogen Energy 44 (2019) 19344.

19. Y. Ding, Y. Wan, Y-L. Min, W. Zhang, S-H. Yu, General synthesis and phase control of metal molybdate hydrates $MMoO_4 \cdot nH_2O$ (M = Co, Ni, Mn, n = 0, 3/4, 1) nano/microcrystals by a hydrothermal approach: magnetic, photocatalytic, and electrochemical properties, Inorganic Chemistry 47 (2008) 7813.

20. L. Cornu, V. Jubera, A. Demourgues, G. Salek, M. Gaudon, Luminescence properties and pigment properties of A-doped (Zn,Mg)MoO_4 triclinic oxides (with A = Co, Ni, Cu or Mn), Ceramics International 43 (2017) 13377.

21. D. Vie, E. Martinez, F. Sapina, J-V. Folgado, A. Beltran, R. X. Valenzuela, V. Corbes-Corberan, Freeze-dried precursor-based synthesis of nanostructured cobalt-nickel molybdates $Co_{1-x}Ni_xMoO_4$, Chem. Mater. 16 (2004) 1697.

22. J. Thrane, L. F. Lundegaard, P. Beato, U. V. Mentzel, M. Thorhauge, A. D. Jensen, M. Hoj, Alkali Earth metal molybdates as catalysts for the selective oxidation of methanol to formaldehyde-selectivity, activity, and stability, Catalysts 10 (2020) 82.

23. Y.-S. Soon, N. Fujikawa, W. Ueda, Y. Moro-oka, K.-W. Lee, Propane oxidation over various metal molybdate catalysts, Catalysis Today 24 (1995) 327.

24. L. M. Madeira, M. F. Portela, C. Mazzocchia, Nickel molybdate catalysts and their use in the selective oxidation of hydrocarbons, Catalysis Reviews 46 (2004) 53.

25. A. P. Vieira Soares, M. Farinha Portela, A. Kiennemann, Methanol selective oxidation to formaldehyde over iron-molybdate catalysts, Catalysis Reviews 47 (2005) 125.

26. L. Zhang, S. Zheng, L. Wang, H. Tang, H. Xue, G. Wang, H. Pang, Fabrication of metal molybdate micro/nanomaterials for electrochemical energy storage, Nano Micro Small 13 (2017) 1700917.

27. P. Li, C. Ruan, J. Xu, Y. Xie, Supercapacitive performance of $CoMoO_4$ with oxygen vacancy porous nanosheet, Electrochim. Acta 330 (2020) 135334.

28. Y-R. Jiang, W. W. Lee, K-T. Chen, M-C. Wang, K-H. Chang, C-C. Chen, Hydrothermal synthesis of β-$ZnMoO_4$ crystals and their photocatalytic degradation of Victoria blue R and phenol, J. Taiwan Institute Chem. Engineers 45 (2014) 207.

29. D. Wang, M. Huang, Y. Zhuang, H-L. Jia, J. Sun, M. Guan, Phase- and morphology-controlled synthesis of zinc molybdate for excellent photocatalytic properties, EurJIC 42 (2017) 4939.

30. L. S. Cavalcante, E. Moraes, M. A. P. Almeida, C. J. Dalmaschio, N. C. Batista, J. A. Varela, E. Longo, M. Siu Li, J. Andres, A. Beltran, A combined theoretical and experimental study of electronic structure and optical properties of β-$ZnMoO_4$ microcrystals, Polyhedron 54 (2013) 13.

31. C. C. Mardare, D. Tanasic, A. Rathner, N. Müller, A. W. Hassel, Growth inhibition of Escherichia coli by zinc molybdate with different crystalline structures, Phys. status solidi A 213 (2016) 1471.

32. N. N. Leyzerovich, K. G. Bramnik, T. Buhrmester, H. Ehrenberg, H. Fuess, Electrochemical intercalation of lithium in ternary metal molybdates $MMoO_4$ (M: Cu, Zn, Ni and Fe), J. Power Sources 127 (2004) 76.

33. J. Fei, Q. Sun, J. Li, Y. Cui, J. Huang, W. Hui, H. Hu, Synthesis and electrochemical performance of α-$ZnMoO_4$ nanoparticles as anode material for lithium ion batteries, Mater. Lett. 198(2017) 4.

34. A. Zitolo, V. Goellner, V. Armel, M-T. Sougrati, T. Mineva, L. Stievano, E. Fonda, F. Jaouen, Identification of catalytic sites for oxygen reduction in iron- and nitrogen-doped graphene materials, Nature Mater. 14 (2015) 937.

35. U. I. Kramm, I. Herrmann-Geppert, J. Behrends, K. Lips, S. Fiechter, P. Bogdanoff, On an easy way to prepare metal-nitrogen doped carbon with exclusive presence of MeN_4-type sites active for the ORR, J. Am. Chem. Soc. 138 (2016) 635.

36. Q. Jia, N. Ramaswamy, U. Tylus, K. Strickland, J. Li, A. Serov, K. Artyushkova, P. Atanassov, J. Anibal, C. Gumeci, S. C. Barton, M-T. Sougrati, F. Jaouen, B. Halevi, S. Mukerjee, Spectroscopic insights into the nature of active sites in iron-nitrogen-carbon electrocatalysts for oxygen reduction in acid, Nano Energy 29 (2016) 65.

37. T. Mineva, I. Matanovic, P. Atanassov, M-T. Sougrati, L. Stievano, M. Clémancey, A. Kochem, J-M. Latour, F. Jaouen, Understanding active sites in pyrolyzed Fe-N-C catalysts for fuel cell cathodes by bridging density functional theory calculations and ^{57}Fe Mössbauer spectroscopy, ACS Catal. 9 (2019) 9359.

38. J. Li, M. T. Sougrati, A. Zitolo, J. M. Ablett, I. C. Oguz, T. Mineva, I. Matanovic, P. Atanassov, Y. Huang, I. Zenyuk, A. Di Cicco, K. Kumar, L. Dubau, F. Maillard, G. Drazic, F. Jaouen, Identification of durable and non-durable FeN_x sites in Fe-N-C materials for proton exchange membrane fuel cells, Nature Catalysis 4 (2021) 10.

39. F. Jaouen, J. P. Dodelet, O_2 Reduction Mechanism on Non-Noble Metal Catalysts for PEM Fuel Cells. Part I: Experimental Rates of O_2 Electroreduction, H_2O_2 Electroreduction, and H_2O_2 Disproportionation, J. Phys. Chem. C 113 (2009) 15422.

40. L. Osmieri, A. H. A. Monteverde Videla, P. Ocon, S. Speccchia, Kinetics of Oxygen Electroreduction on Me–N–C (Me = Fe, Co, Cu) Catalysts in Acidic Medium: Insights on the Effect of the Transition Metal, J. Phys. Chem. C 121 (2017) 17796.

41. J. Chlistunoff, RRDE and Voltammetric Study of ORR on Pyrolyzed Fe/Polyaniline Catalyst. On the Origins of Variable Tafel Slopes, J. Phys. Chem. C 115 (2011) 6496.

42. Y-C. Ma, Y-H. Zhu, X-F. Tang, L-F. Hang, W. Jiang, M. Li, M. I. Khan, Y-Z. You, Y-C. Wang, Au nanoparticles with enzyme-mimicking activity-ornamented ZIF-8 for highly efficient photodynamic therapy, Biomater. Sci. 7, (2019) 2740.

43. L. Song, C. Huang, W. Zhang, M. Ma, Z. Chen, N. Gu, Y. Zhang, Graphene oxide-based Fe_2O_3 hybrid enzyme mimetic with enhanced peroxidase and catalase-like activities, Colloids and Surfaces A: Physicochem. Eng. Aspects 506 (2016) 747.

44. Y. Huang, J. Ren, X. Qu, Nanozymes: classification, catalytic mechanisms, activity regulation, and applications, Chem. Rev. 119 (2019) 4357.

45. J. Fan, J-J. Yin, B. Ning, X. Wu, Y. Hu, M. Ferrari, G. J. Anderson, J. Wei, Y. Zhao, G. Nie, Direct evidence for catalase and peroxidase activities of ferritin-platinum nanoparticles, Biomater. 32 (2011) 1611.

46. J. Mu, Y. Wang, M. Zhao, L. Zhang, Intrinsic peroxidase-like activity and catalase-like activity of Co_3O_4 nanoparticles, Chem. Commun. 48 (2012) 2540.

47. J. Mu, L. Zhang, M. Zhao, Y. Wang, Catalase mimic property of Co_3O_4 nanomaterials with different morphology and its application as a calcium sensor, ACS Appl. Mater. Interfaces 6 (2014) 7090.

48. Z. Chen, J-J. Yin, Y-T. Zhou, Y. Zhang, L. Song, M. Song, S. Hu, N. Gu, Dual enzyme-like activities of iron oxide nanoparticles and their implication for diminishing cytotoxicity, ACS Nano 6 (2012) 4001.

49. J. Baltrusaitis, B Mendoza-Sanchez, V. Fernandez, R. Veenstra, N. Dukstiene, A. Roberts, N. Fairley, Generalized molybdenum oxide surface chemical state XPS determination via informed amorphous sample model, Applied Surface Science 326 (2015) 151.

50. J-G. Choi, L.T. Thompson, XPS study of as-prepared and reduced molybdenum oxides, Applied Surface Science 93 (1996) 143.

51. A. Zitolo, N. Ranjbar-Sahraie, T. Mineva, J. Li, Q. Jia, S. Stamatin, G. F. Harrington, S. M. Lyth, P. Krtil, S. Mukerjee, E. Fonda, F. Jaouen, Nature Communications 8 (2017) 957.